

PRECISE INFRARED RADIAL VELOCITIES FROM KECK/NIRSPEC AND THE SEARCH FOR YOUNG PLANETS

JOHN I. BAILEY, III¹

University of Alabama Huntsville, Physics Department, 301 Sparkman Drive, 201B Optics Building, Huntsville, AL 35899

RUSSEL J. WHITE

Georgia State University, Department of Physics and Astronomy, 29 Peachtree Center Avenue, Science Annex, Suite 400, Atlanta, GA 30303

CULLEN H. BLAKE

Department of Astrophysical Sciences, Princeton University, Peyton Hall, Ivy Lane, Princeton, NJ 08544

DAVE CHARBONNEAU

Harvard-Smithsonian Center for Astrophysics, 60 Garden Street, Cambridge, MA 02138

TRAVIS S. BARMAN

Lowell Observatory, 1400 West Mars Hill Road, Flagstaff, AZ 86001

ANGELLE M. TANNER

Georgia State University, Department of Physics and Astronomy, 29 Peachtree Center Avenue, Science Annex, Suite 400, Atlanta, GA 30303

AND

GUILLERMO TORRES

Harvard-Smithsonian Center for Astrophysics, 60 Garden Street, Cambridge, MA 02138

to appear in ApJ

ABSTRACT

We present a high-precision infrared radial velocity study of late-type stars using spectra obtained with NIRSPEC at the W. M. Keck Observatory. Radial velocity precisions of 50 m/s are achieved for old field mid-M dwarfs using telluric features for precise wavelength calibration. Using this technique, 20 young stars in the β Pic (age ~ 12 Myr) and TW Hya (age ~ 8 Myr) Associations were monitored over several years to search for low mass companions; we also included the chromospherically active field star GJ 873 (EV Lac) in this survey. Based on comparisons with previous optical observations of these young active stars, radial velocity measurements at infrared wavelengths mitigate the radial velocity noise caused by star spots by a factor of ~ 3 . Nevertheless, star spot noise is still the dominant source of measurement error for young stars at $2.3 \mu\text{m}$, and limits the precision to ~ 77 m/s for the slowest rotating stars ($v \sin i < 6$ km/s), increasing to ~ 168 m/s for rapidly rotating stars ($v \sin i > 12$ km/s). The observations reveal both GJ 3305 and TWA 23 to be single-lined spectroscopic binaries; in the case of GJ 3305, the motion is likely caused by its $0''.09$ companion, identified after this survey began. The large amplitude, short-timescale variations of TWA 13A are indicative of a hot Jupiter-like companion, but the available data are insufficient to confirm this. We label it as a candidate radial velocity variable. For the remainder of the sample, these observations exclude the presence of any 'hot' ($P < 3$ days) companions more massive than $8 M_{Jup}$, and any 'warm' ($P < 30$ day) companions more massive than $17 M_{Jup}$, on average. Assuming an edge-on orbit for the edge-on disk system AU Mic, these observations exclude the presence of any hot Jupiters more massive than $1.8 M_{Jup}$ or warm Jupiters more massive than $3.9 M_{Jup}$.

Keywords: stars: pre-main sequence — starspots — planets and satellites: formation — techniques: radial velocities — techniques: spectroscopic — methods: data analysis

baileyji@umich.edu
 white@chara.gsu.edu

¹ Current Address: Department of Astronomy, University of Michigan, 830 Dennison Building, 500 Church Street, Ann Arbor, MI 48109

⁶ Current Address: Mississippi State University, Department of Physics and Astronomy, 355 Lee Boulevard, Hilbun Hall,

Starkville, MS 39762

1. INTRODUCTION

The remarkable discovery of extrasolar planets orbiting sun-like stars in 1995 was accomplished by utilizing novel techniques that improved the radial velocity (RV) precision by two orders of magnitude (from ~ 1 km/s to 10 m/s), which was at last sufficient to search for the slight gravitational wobble induced by an orbiting gas giant planet upon its host star (Walker et al. 1995; Mayor & Queloz 1995; Marcy & Butler 1996; Cochran et al. 1997; but cf. Latham et al. 1989). Since then an extensive international effort has begun to determine the ubiquity and basic properties of these initially elusive objects. Based on a modest extrapolation of current findings, we now know that roughly 12% of Sun-like stars (F, G, and K spectral type) harbor gas giant planets within 30 AU (e.g. Butler et al. 2006; Udry et al. 2007; Cumming et al. 2008; Wright et al. 2010; Howard et al. 2010). While the masses of these planets are similar to the gas giants in our solar system (i.e. Jupiter and Saturn), their orbital properties are in many ways radically different. Some orbit their host star in just a few days time (the “hot Jupiters”), while others have highly eccentric orbits. Planet-like companions have even been directly imaged at separations of more than 100 AU from their host star (Kalas et al. 2008).

The dramatically different properties of extrasolar planets compared to those in our solar system forced theorists to reconsider the standard paradigm for gas giant planet formation. Now, planet formation scenarios generally fall into 2 categories, core accretion (Mizuno et al. 1980) and disk instabilities (Boss 1997). Core accretion is the favored mechanism for producing giant planets with large core masses (e.g. Sato et al. 2005) and can naturally explain the enhanced frequency of planets around metal rich stars (e.g. Robinson et al. 2006). However, at wide separations ($\gtrsim 10$ AU) the timescale for planet formation via core accretion (Pollack et al. 1996; Alibert et al. 2005) is longer than the typical disk dissipation timescale ($\lesssim 10$ Myr; Haisch 2001; Briceño et al. 2001; Carpenter et al. 2006; Pascucci et al. 2006); it is thus an unlikely formation mechanism for the planets in very wide orbits about Fomalhaut and HR 8799 (Marois et al. 2008; Kalas et al. 2008). Disk instabilities, on the other hand, can form planets much more quickly ($\lesssim 1$ Myr), well before circumstellar disks are dispersed (Boss 1997, 2004; Mayer et al. 2002; Meru & Bate 2010, but cf. Stamatellos & Whitworth 2008; Meru & Bate 2011). This mechanism also works nearly as efficiently around low mass stars, with sufficiently massive disks, and seems a more plausible scenario for forming the known massive planets orbiting M dwarfs (Boss 2006). Of course, it is possible that both scenarios operate or dominate within different regimes of stellar and/or disk mass.

In addition to the uncertainties surrounding planet formation, it is also unclear how the orbits of newly formed planets dynamically evolve. Since giant planets are believed to form beyond the snowline (e.g. Kennedy & Kenyon 2008), inward orbital migration must occur in many systems to explain the wealth of short period planets; roughly 10% of gas giant planets have separations less than 0.1 AU (Butler et al. 2006). Interactions with disk material is widely be-

lieved to be the most efficient mechanism for inward migration (e.g. Goldreich & Tremaine 1980; Lin et al. 1996). If most gas giants migrate via this process, the hot Jupiters must become ‘hot’ within ~ 10 Myr after formation, prior to disk dissipation. However, planet-disk interactions typically circularize orbits and maintain spin-orbit alignment with the star, so other processes such as dynamical scattering with other planets (Adams & Laughlin 2003; Raymond et al. 2011) or a nearby star (Malmberg et al. 2007; Malmberg & Davies 2009) may be needed to produce the broad extrasolar planet eccentricity distribution and the spin-orbit misalignments of many transiting planets (e.g. Pont et al. 2009). These dynamical interactions could take many hundreds of millions of years (e.g. see review by Lubow & Ida 2010).

One direct way to begin constraining the mechanisms and timescales of planet formation and migration is to search for planets around stars with ages of $\lesssim 10$ Myr, or essentially immediately after planets could have formed. Direct imaging searches for planets have been more successful at this recently than RV searches. Several massive Jupiter-like companions have been directly imaged around stars with these ages, though at somewhat wide separations (10 to many 100s of AU; e.g. Neuhäuser et al. 2005; Lagrange et al. 2010; Ireland et al. 2011); these important discoveries are helping to motivate future high-contrast imaging facilities and the science achievable with them (e.g. Macintosh et al. 2008; Kataria & Simon 2010). In many cases, however, planetary status relies upon comparisons with poorly tested evolutionary models, and the wide separations offer little constraint on the migration mechanism responsible for forming hot Jupiter-like planets.

Planets identified via RV variations, on the other hand, yield immediate mass lower limits ($m \sin i$) and preferentially find massive short-period planets which most likely have migrated. However, two universal properties of young stars inhibit measuring their RV precisely at optical wavelengths, and consequently they are often excluded in high precision RV surveys for planets. The first of these is that young Sun-like stars are much cooler while young, and thus fainter at optical wavelengths. A 1 solar mass star, for example, has a spectral type of $\sim K5$ at 10 Myr (Baraffe et al. 1998; Siess et al. 2000). This, coupled with the fact that all star forming regions are further away than 100 pc means that most young stars are simply too faint for high-precision RV work at optical wavelengths. The second of these is that young stars are often modestly to rapidly rotating. This rotation broadens stellar absorption features and, even more perniciously, generates chromospheric activity and a spotted stellar surface. Several pioneering RV studies of young spotted stars have shown that their presence can induce low amplitude, periodic RV shifts, and thus mimic the effect of one or more orbiting planets (Queloz et al. 2001; Paulson & Yelda 2006; Huerta et al. 2008; Prato et al. 2008; Reiniers et al. 2010; Crockett et al. 2011; Mahmud et al. 2011); amplitudes of 200 - 700 m/s have been observed. In a couple cases, Jupiter-like companions have been reported orbiting young stars based on low-amplitude (< 1 km/s) RV variations (Setiawan et al. 2008;

Hernán-Obispo et al. 2010), but subsequent observations indicate that these too were misidentifications caused by star spots (Huélamo et al. 2008; Figueira et al. 2010).

One promising way to overcome these observational challenges is to observe at infrared wavelengths. As has been demonstrated, modern infrared spectrographs utilizing molecular gas cells are able to obtain RV precisions comparable to very stable optical facilities (e.g. Bean et al. 2010). This wavelength range is advantageous for young stars on cool convective tracks since it is much closer to the peak of their energy distribution, thereby improving observing efficiency. More significantly, at these wavelengths the contrast between the photosphere and cool star spots is reduced; this is confirmed by the decline in the photometric variability of spotted stars with wavelength (e.g. Herbst et al. 1994). Since the RV “noise” induced by star spots is directly proportional to the amplitude of a star’s photometric variability (Saar & Donahue 1997), the diminished variability at longer wavelength observations should help mitigate the noise of star spots. Observations of young spotted stars at both optical and infrared wavelengths appear to confirm this prediction (Prato et al. 2008; Huélamo et al. 2008; Mahmud et al. 2011).

Motivated by the prospects for obtaining high-precision RV measurements of young stars at infrared wavelengths, in late 2004 we began an ambitious observational program at the W. M. Keck Observatory (PI: R. White) to search for young planets. Here we present initial results. In Section 2 we describe the sample selection and in Section 3 we summarize the acquisition of infrared spectra. In Sections 4 and 5 we describe our method for optimally extracting the spectra and for modeling the spectra to determine precise RVs. The results of this survey, which include the discovery of two spectroscopic binaries and one candidate hot Jupiter, are highlighted in Section 6. In Section 7 we determine detection limits for the ensemble sample via Monte Carlo simulations and quantify the advantage infrared RVs measurements have over optical measurements for young stars. Our overall findings are summarized in Section 8.

2. THE OBSERVATIONAL SAMPLE: YOUNG STARS AND COMPARISON FIELD STARS

Although our entire young star survey includes stars from both star forming regions and nearby loose associations, in this first paper we focus only on young stars in the β Pic and TW Hydrae Associations, which have ages of ~ 12 Myr and ~ 8 Myr, respectively (Torres et al. 2008). The high quality spectra of these nearby, systematically brighter stars were our initial focus as we developed techniques for precise RV measurements. The selection criteria for targets within these associations were that the star have no known companions within $2''0$, be somewhat slowly rotating ($v \sin i \lesssim 15$ km/s, if known), show no signs of accretion (e.g. TW Hya itself was excluded), and have an M spectral type. The spectral type criterion was adopted to ensure that stars have strong ^{12}CO R-branch lines in their spectra, from which RVs are measured. Stars were selected from the membership lists assembled in Zuckerman & Song (2004); 9 stars from the β Pic Association and 9 stars from the TW Hydrae Association met these criteria. Wide companions

to 2 of these stars have spectral types just slightly earlier than M, AG Tri A (K6) and TWA 9A (K5), and were therefore also included since their acquisition overhead would be minimal. Spectroscopic observations of a few of these stars (GJ 871.1 B, TWA 12, TWA 23) revealed that they were more rapidly rotating than our initial selection criterion. We nevertheless continued to observe these stars in order to investigate empirically how the precision degrades with projected rotational velocity.

After our observational program began, one of our targets, GJ3305, was discovered to be a $0''093$ binary (Kasper et al. 2007), making it a triple star system (Feigelson et al. 2006). It was consequently observed less often as it was considered a less likely planet host. We also note that of the 20 young stars in this sample, 14 of them (70%) are members of wide binary star systems, with separations ranging from 29 to 1967 AU. These include AG Tri A and B, GJ 799 A and B, GJ 871.1 A and B, GJ3305, TWA 8A and 8B, TWA 9A and 9B, TWA 11B, TWA 13A and 13B.

In addition to these 20 young stars, we also included in our sample the well studied single M dwarf flare star GJ 873 (EV Lac). GJ 873 is the second brightest M dwarf X-ray source in the *Röntgensatellit* All-Sky Survey (Hünsch et al. 1999; Osten et al. 2006), has one of the strongest surface magnetic field strengths measured on an M dwarf (Johns-Krull & Valenti 1996; Reiners & Basri 2007), and a differential star spot covering factor of 4-11% (Abranin et al. 1998). While its activity suggests a young age, its dwarf-like gravity and the absence of lithium in its atmosphere (Pettersen et al. 1984) indicate it is not pre-main sequence. It’s usually classified as a young disk star (e.g. Osten et al. 2006) with an approximate age of 10^8 yr. The motivation for including this star was to assess the achievable RV precision at infrared wavelengths in the limit of extreme surface activity.

For calibration purposes we observed a handful of A spectral type stars during each observing run. The telluric absorption features superimposed upon these nearly featureless stellar spectra, at infrared wavelengths, are used to characterize the instrumental profile. In addition, we observed 3 mid-M dwarf stars (GJ 628, GJ725A and GJ725B) that have been previously monitored with high precision optical RV techniques and shown to have no detectable RV companions (Nidever et al. 2002; Endl et al. 2006); Endl et al. (2006) measure RV dispersions of 7.4 m/s and 7.1 m/s for GJ 725A and GJ 725 B, respectively. These stars were included to assess the achievable RV precision in the limit of slowly rotating, inactive stars.

Stellar masses for the young stars are estimated by comparing their stellar temperatures to a theoretical isochrone. To do this we assembled stellar spectral types from original references (see Table 1) and assigned temperatures using the T Tauri-like temperature scale of Luhman (2003) for stars cooler than M0, and the dwarf temperature scale of Kraus & Hillenbrand (2007) for hotter stars. These temperatures are then compared to the 10 Myr isochrone of Baraffe et al. (1998) with a mixing length of 1.9 above $0.6 M_{\odot}$ and a mixing length of 1.0 at lower masses; this evolutionary model with the adopted temperature scale is consis-

Table 1
Observed Sample

Star Name	SpT	Reference	K (mag)	Mass (M_{\odot})	Period ($days$)	Reference	$v \sin i$ (km/s)	Reference
Single Field Stars								
GJ 628	M3.5	H94	5.07	0.30	< 1.1	D98
GJ 725A	M3	H94	4.43	0.37	< 2.8	D98
GJ 725A	M3.5	H94	5.00	0.30	< 2.8	D98
Chromospherically Active Field Stars								
GJ 873	M3.5	H94	5.30	0.30	4.38	M95
β Pic Stars								
AU Mic	M0	H96	4.53	0.73	4.87	M95	8.5	S07
AG Tri A	K6	S03	7.08	0.94	13.7	N07
AG Tri B	M0	S03	7.92	0.73
GJ 182	M0	H96	6.26	0.73	4.56	M95
GJ 3305	M0.5	H96	6.41	0.67	6.10	F06	5.3	S07
GJ 799 A	M4.5	H96	5.69	0.16	10.6	S07
GJ 799 B	M4	H96	5.69	0.22	17.0	S07
GJ 871.1 A	M4	S02	6.93	0.22	2.355	M10	14.0	S07
GJ 871.1 B	M4.5	S02	7.79	0.16	24.3	S07
HIP 12545	M0	S03	7.07	0.73	1.25	M10	9.3	S07
TW Hya Stars								
TWA 7	M1	W99	6.90	0.60	5.05	LC05	< 5	S07
TWA 8A	M2	W99	7.43	0.51	4.65	LC05	< 5	S07
TWA 8B	M5	W99	9.01	0.12	0.78	LC05	11.2	S07
TWA 9A	K5	W99	7.85	1.01	5.10	LC05	11.3	S07
TWA 9B	M1	W99	9.15	0.60	3.98	LC05	8.4	S07
TWA 11B	M2.5	W99	8.35	0.44	12.1	S07
TWA 12	M2	S99	8.05	0.51	3.28	LC05	16.2	S07
TWA 13A	M1	S99	7.49	0.60	5.56	LC05	10.5	S07
TWA 13B	M2	S99	7.46	0.51	5.35	LC05	14.8	S07
TWA 23	M1	S03	7.75	0.60

Note. — References: D98 = Delfosse et al. (1998), F96 = Feifelson et al. (2006), H94 = Henry et al. (1994), H96 = Hawley et al. (1996), LC05 = Lawson & Crause (2005), M95 = Mathioudakis et al. (1995), N07 = Norton et al. (2007), S02 = Song et al. (2002), S03 = Song et al. (2003), S07 = Sholtz et al. (2007), W99 = Webb et al. (1999)

tent with the available dynamical mass constraints for young stars (Hillenbrand & White 2004; Mathieu et al. 2007). This yields stellar masses that range from 0.12 M_{\odot} to 1.01 M_{\odot} , with a median mass of 0.6 M_{\odot} . Approximate masses for the field dwarfs are estimated from the absolute magnitude - mass relations of Henry & McCarthy (1993), where the absolute magnitudes have been assigned based on spectral type relations given in Kraus & Hillenbrand (2007).

Table 1 summarizes the basic properties of the sample observed, excluding the A spectral type stars. The listed properties include spectral types, K magnitudes, mass estimates, rotational periods, if known, previously reported $v \sin i$ values, if available, and the corresponding references. The K magnitudes for the field stars are taken from Leggett (1992) whereas the values for Association members are from the 2MASS survey, and thus are K_s magnitudes. Since the 2MASS survey reports only a combined magnitude for GJ799AB, a 2''8 pair, we estimate each component's magnitude by assuming they are equally bright; the components of this binary have the same spectral type.

3. HIGH DISPERSION INFRARED SPECTRA

Spectroscopic observations of the sample stars were obtained using the cross-dispersed infrared echelle spectro-

graph NIRSPEC (McLean et al. 1998) on the W. M. Keck II telescope. The observations were obtained over 12 observing runs in total, spanning from 2004 Nov 16 to 2009 May 12. The large number of runs was a consequence of this program being completed in concert with a similar program focused on L dwarfs (Blake et al. 2007, 2010).

All observations were obtained with the 3 pixel (0''.432) slit in combination with the N7 blocking filter, and approximate echelle angle 62.65 and grating angle 35.50. This yielded 7 orders of spectra spanning approximately 1.99 μm to 2.39 μm , with gaps between the orders, at a resolving power of approximately 30,000 (measured as described below). The spectra were obtained in pairs at two locations along the slit. Collecting observations in this manner provided a nearly simultaneous measurement of sky emission and detector bias for both images.

Since the measurement goal of this program was precise RVs, considerable effort was put into maintaining instrument stability by not moving any internal components of NIRSPEC while observing. However, when the NIRSPEC software is first started (at the beginning of a night) or when a software crash occurs, the motors for the filter wheels and reflection angles must all be reinitialized, forcing the internal components to move. Since re-

setting the reflection angles typically results in a slightly different setting, these values were tweaked slightly, by eye, to return to the primary wavelength setting; this procedure resulted in the same wavelength coverage to within a few pixels. Since the spectroscopic properties of this new setting would be slightly different, we strived to characterize each ‘observational set’ by intensively observing one of the A spectral type stars for each NIR-SPEC setting. We were successful in this effort for all but one ‘observational set’.

4. IMAGE REDUCTION AND SPECTRAL EXTRACTION

For each observational set, described above, dark images were median combined and this median was subtracted from each flat-field image. These subtracted flat-field images were then normalized by counts in the central $\sim 10\%$ of the array, and then median combined to generate a master flat. Regions outside the illuminated 7 orders were set to unity. The orders were not normalized in the direction of dispersion, a necessary step to strictly preserve the counts and the correct relative signal-to-noise ratio (SNR); skipping this led to fringing effects that were more consistent, smaller in amplitude, and easier to remove (see below). All spectrum images were then divided by the master flat constructed for its observational set, and then each flattened image had its corresponding nod image subtracted from it to remove the sky emission, detector bias and dark current. This yielded 2 reduced spectrum images for each epoch.

Prior to spectral extraction, the 7 spectral orders were located on the reduced spectrum image automatically by finding maxima in smoothed spatial profiles of each order (i.e. perpendicular to the dispersion direction). Gaussian functions were then fit to these spatial profiles in binned segments of 10-columns along the orders. The orders were then traced by fitting a low order polynomial to the peak position of these Gaussians, with 3σ outliers excluded from the fit. Next, regions that were more than 3 sigma above or below the best fit polynomial defining the center of each order were masked and excluded from any further analysis. Masking the orders in this way objectively accounted for variations in the spatial width of the spectra, usually caused by variations in the seeing, and proved vital for successful extraction of pair subtracted spectra only $10''0$ apart.

Spectra were extracted from the masked images using a modified version of the ‘optimal extraction’ procedure described in Horne et al. (1986). Unlike standard extraction techniques which simply sum pixel values over a specified range, optimal extraction sums pixels weighted by the variance of an assumed smoothly varying spatial profile that can be defined either perpendicular to or parallel to the dispersion direction. This minimizes the noisy contributions of profile wings and allows significant deviates from the profile (e.g. hot pixels and cosmic rays) to be easily identified and removed (see Piskunov & Valenti 2002 for this and other issues related to the optimal extraction of cross-dispersed echelle spectra). After considerable experimentation, we adopted spatial profiles defined parallel to the dispersion direction and used a Gaussian plus second order polynomial to model these. The variance of the profile was determined from each pair subtracted flat-fielded spectrum image. We note that this is slightly different from the recommendation of

Horne et al. (1986) to use a bias subtracted flat-fielded spectrum image; as with most infrared observations, the bias is only removed as a part of pair subtraction. The addition of these bias counts produced slightly larger variance estimates, but this yielded no noticeable effect on our relatively high SNR spectra. Future studies may consider obtaining bias images throughout the night in an attempt to determine a more accurate variance image.

An example of an optimally extracted spectrum is shown in Figure 1. One feature not accounted for in these extractions is interference fringing. Although some investigators have developed prescriptions to remove this via Fourier filtering (Deming et al. 2005), we accounted for this feature in the spectral modeling process.

5. MODELING THE SPECTRA AND PRECISE RADIAL VELOCITY MEASUREMENTS

5.1. Assumptions

Precise RVs were extracted from the observations by constructing a detailed model of each spectrum. Although a wide variety of modeling prescriptions were investigated with our data to optimize this, the prescription described here is the one that yielded the most consistent RVs for 15+ epochs of 3 slowly rotating M dwarfs with no known planets (GJ 628, GJ725A and GJ725B).

The modeled spectra were constructed from an ultra-high resolution KPNO/FTS telluric spectrum, extracted from observations of the Sun (Livingston & Wallace 1991), and synthetically generated stellar spectra, computed from updated and improved NextGen models (Hauschildt et al. 1999), constructed and provided by coauthor T. Barman. Although the ^{12}CO bandhead and R branch lines are temperature and surface gravity dependent, we did not determine these parameters from our spectra; attempts to do this yielded results that were only marginally consistent with previous values considered to be more accurate (e.g. from optical spectra). Instead, we used a synthetically generated spectrum that most closely matched each star’s spectral type and expected surface gravity. All field stars (GJ 628, GJ725A, GJ725B, GJ 873) were assumed to have a $\log(g) = 4.8$ dex, while the young stars were assumed to have a $\log(g) = 4.2$ dex, consistent with recent $\log(g)$ measurements (Mentuch et al. 2008). The stellar properties of the spectral templates used for each star are listed in Table 2.

Each observation was modeled by combining a telluric and a synthetic spectrum, parametrized by 10 free parameters. Four parameters determine instrumental properties - the wavelength solution was parametrized by a quadratic polynomial, characteristic of slightly curved spectral orders, and the instrumental spectral profile was modeled as a single best-fit Gaussian for the entire order. The remaining six parameters characterize the spectral properties, including the depth of telluric features, the depth of stellar features, the star’s projected rotational velocity ($v\sin i$), a linear (2 parameter) continuum normalization offset, and finally, the star’s RV. The limb darkening coefficient used to calculate rotationally broadened profiles, which was *not* considered a free parameter in these calculations, was held fixed at 0.6 in all cases.

5.2. Implementation

Only 1 of the 7 orders acquired (NIRSPEC order #33) was modeled; this is one of the few wavelength regions which has a sufficiently rich array of both the stellar and telluric absorption features, permitting precise RV calibration. The usable region of the observed order spans approximately 270 Å, from 2.288 μm to 3.315 μm (Figure 1).

The spectral modeling proceeded in essentially 3 stages. First, the A-type star spectra were modeled to construct initial estimates of the wavelength solution and instrumental profile for each observational set. Since the spectra of A type stars are essentially featureless over this wavelength range, their spectra were modeled as simple telluric spectra, and 3 of the 10 parameters of the general fit were omitted (stellar absorption depth, $v\sin i$, and RV). The best fit was determined by subtracting the model spectrum from the observed spectrum and applying a Hamming filter to this difference to remove the residual fringing pattern. Optimization was achieved by an iterative process that minimized the variance-weighted reduced χ^2 of these filtered residuals, using the prescription described below. Parameters determined for multiple A star observations within a set were averaged, weighted by their χ^2 values, to determine the best “first guess” values for that set.

The average best fit instrumental profile determined from the best fit models of the A star spectra corresponded to a resolving power of $\sim 30,000$, with a dispersion of $\sim 2,000$. This is larger than expected for this instrumental setup, which is predicted to yield resolving powers of $\sim 25,000$ (McLean et al. 1998). Although we are unsure of the discrepancy, it may be attributable to the excellent seeing at Mauna Kea and starlight not fully filling the 0.432 slit.

Each late-type stellar spectrum was modeled by adopting and holding fixed its set’s estimates of the linear and quadratic terms of the wavelength solution. All other parameters were determined via an iterative fitting process, but at all times the parameters were nevertheless restricted to realistic ranges. In the first iteration the 0th order component of the wavelength solution was optimized by allowing it to vary; the parameter describing the instrument profile was adopted from its set’s estimate. The second iteration optimized the instrument profile by allowing it to vary. The third iteration was used to determine the stellar $v\sin i$ by allowing it to vary. Once complete, a chi-square weighted mean of the best-fit $v\sin i$ value was computed and adopted for the star. In the final iteration only the 5 remaining parameters (2 normalization parameters, telluric depths, stellar depths, RV) were allowed to vary.

For the 1 observational set without any A star observations (Section 3), the target stars of that set were modeled using the average A star parameters from all other sets as a first guess. The analysis then proceeded as described above. The agreement of measured stellar properties (e.g. RVs, $v\sin i$) from this set and other sets suggested the lack of A stars did not compromise the analysis in this case, likely because of the nearly identical observing setups carefully determined each time.

The specific prescription used to determine multiple-parameter best fits can have a significant impact on the results. In this first study we adopted a minimization of

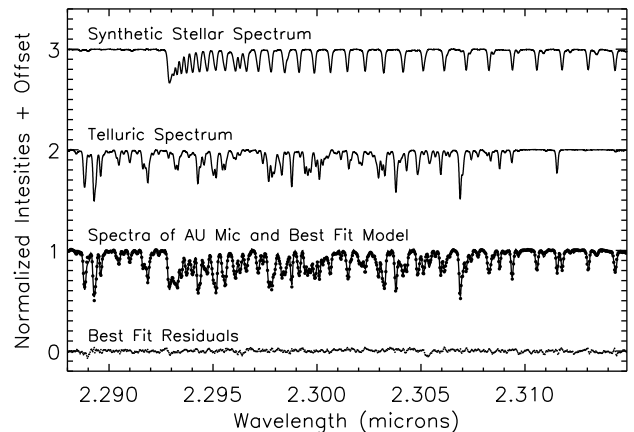


Figure 1. Illustration of the procedure to derive precise radial velocities using NIRSPEC data. A telluric spectrum (*top spectrum*) is combined with a synthetic stellar spectrum (*2nd spectrum*) to construct a model spectrum (*3rd spectrum*, dotted line; difficult to see) that is optimized to match an observed spectrum of AU Mic (*3rd spectrum*, solid line). The normalized dispersion of the best fit residuals (*4th spectrum*) is 1.5%, and is characteristic of the majority of our fits.

the filtered difference spectra based on the downhill simplex method of Nelder & Mead (1965), as implemented by Press et al. (1992)³. Our implementation of this prescription enforced user-specified limits on each parameter by restarting an iteration with new parameters if any were out of bounds. The minimization proceeded until both the best fit χ^2 dropped by less than one percent and all parameters remain consistent with recent values.

Figure 1 shows an example model spectrum for comparison with the observed spectrum of the young star AU Mic. The residuals to the fit have a normalized dispersion of 1.5%, which is typical for the majority of modeled spectra. We note that the results from this last stage yield absolute RVs, since they are determined relative to *at rest* telluric absorption features. These values are then converted to barycentric velocities using a correction prescription accurate to ~ 1 m/s (G. Basri; priv. comm.). For the interested reader, we note that Seifahrt et al. (2008), Blake et al. (2010), Bean et al. (2010), Crockett et al. (2011) and Muirhead et al. (2011) provide detailed descriptions of complementary methods to determine precise RVs with nod-subtracted infrared spectra.

6. RESULTS

In Table 2 we summarize the results of our spectroscopic modeling effort to extract RVs. The second column lists the synthetic model parameters (T_{eff} , $\log(g)$) assigned in the spectral fits to each star, and the third column lists the determined $v\sin i$ values. Uncertainties in the $v\sin i$ values are set to be the standard deviation of the $v\sin i$ estimates using all epochs for each star and thus are not necessarily free of systematic effect. The very large uncertainty for TWA 23 may be a consequence of its spectroscopic companion (Section 6.2) broadening its line profiles in some epochs.

The fourth column in Table 2 lists the mean RV and

³ The version of this multiple-parameter optimization available in the IDL Astronomy User’s Library, called *AMEOBA*, must be converted to double-precision to converge self-consistently.

the uncertainty in this mean (σ/\sqrt{N}), calculated from all observations. The uncertainties in the mean range from 12 m/s to 65 m/s for single stars; these are some of the most precise absolute system RV measurements ever for young stars. The fifth and sixth columns list the number of observations (N) and the standard deviation (σ) of the RV measurements extracted from these observations. In the following analysis, we include GJ 873 in the statistics determined for young stars.

In the Appendix, RV measurements from each epoch for all stars are provided. The calculation of the measurement uncertainties are describe below. Figure 2 illustrates several RV curves, including the field star GJ725 A (M3.5), the flare star GJ 873 (M3.5), the debris disk host AU Mic, and the components of the wide binary TWA 8.

In the following sections the ensemble RV dispersions, as measured by the standard deviations, are used to assess empirically the precision with which RVs can be measured and to identify RV variables.

6.1. Error Analysis

For single stars, the RV dispersions are assumed to stem from 3 causes of variability: (1) a theoretical photon noise error (σ_{phot}) based on the SNR of the observed spectrum and the number and shape of the features in best-fit synthetic and telluric spectra, (2) an instrumental error (σ_{inst}) based on the characteristics of NIRSPEC spectra, and (3) an intrinsic stellar error (σ_{stel}) caused by stellar activity. Although the second and third causes are likely attributable to non-stochastic events (e.g. variable bias, fringing or stellar flares, star spots, respectively), we nevertheless assume that these variability sources add in quadrature to produce the observed dispersions ($\sigma_{obs}^2 = \sigma_{phot}^2 + \sigma_{inst}^2 + \sigma_{stel}^2$).

Observations of the 3 slowly rotating single field stars are used to quantify the magnitude of σ_{inst} . As noted in Section 2, previous precise RV measurements of these stars show that their σ_{stel} is small (< 10 m/s); we assign values of zero for all 3 stars. The σ_{phot} values are calculated for each pair averaged observation using the SNR and a prescription similar to that outlined in Butler et al. (1996). Essentially this error term is computed as the photon-limited Doppler error of the best fit synthetic spectrum added in quadrature with the photon-limited wavelength error of the best fit telluric spectrum. Because we successfully achieved similar high SNRs for all observations, the median pair-averaged σ_{phot} for the 3 field stars are similar (26.2 m/s, 26.4 m/s, 27.1 m/s). We use these to estimate σ_{inst} by removing the photon noise error σ_{phot} from the observed dispersion values ($\sigma_{inst}^2 = \sigma_{obs}^2 - \sigma_{phot}^2$). The σ_{inst} values for these 3 stars are consistent to within 4 m/s, with a median of 46 m/s. These values are only slightly smaller than their observed dispersions, as expected for high SNR spectra of inactive stars. We note that a possible error term not accounted for in these calculations is the stability of the telluric features used for calibration. However, optical (Cochran et al. 1988) and infrared (Seifahrt et al. 2010) RV studies conducted with other facilities have shown these features to be stable to $\lesssim 10$ m/s; their stability is thus not a limiting factor for precisely measured RVs with NIRSPEC. These results imply that achieving RV precisions significantly better than ~ 40 m/s

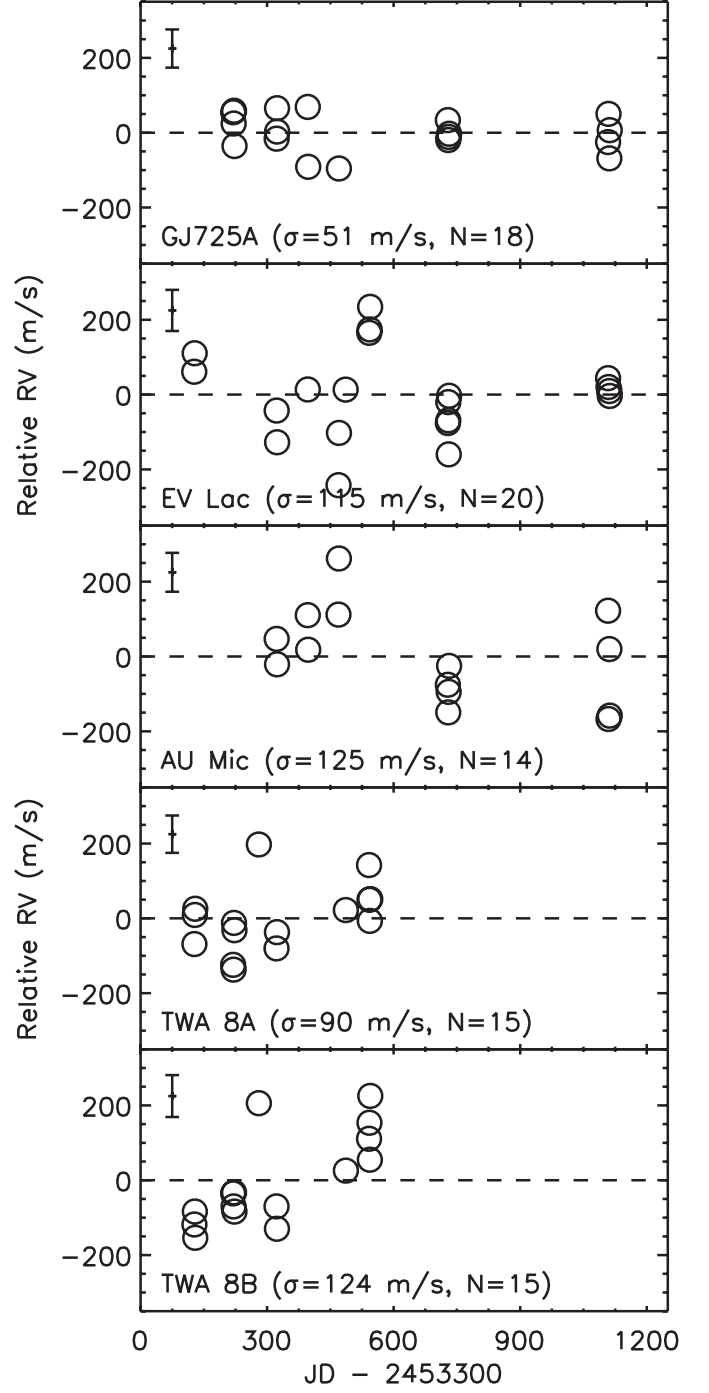


Figure 2. RV curves for the slowly rotating single field star GJ725 A, the chromospherically active star GJ 873, the debris disk host AU Mic, and the components of the wide binary TWA 8; average errorbars are illustrated in the upper left of each panel. The dispersions of the field stars, like GJ 725 A, demonstrate an observing precision of ~ 50 m/s using high SNR spectra of slowly rotating inactive stars. The larger dispersions of other stars are primarily a consequence of enhanced stellar activity.

with NIRSPEC will be challenging unless some methods are developed to account for the instrumental noise, which we presume is attributable to the features of its 1990s generation array (McLean et al. 1998, e.g. read noise, fringing). It is also possible that some improvements may be realized using alternative spectral modeling techniques that incorporate template spectra in-

Table 2
Survey Results

Star Name	Model $T_{eff}, \log(g)$	$v \sin i$ (km/s)	$< RV >$ (m/s)	N	σ_{obs} (m/s)	3d (M_J)	10d (M_J)	30d (M_J)	100d (M_J)
Single Field Stars									
GJ 628	3400, 4.8	1.7 ± 0.1	-21113 ± 15	13	55	3.7	5.3	8.7	10.5
GJ 725A	3400, 4.8	1.8 ± 0.1	-611 ± 12	18	51	5.0	6.9	13	16
GJ 725B	3400, 4.8	1.8 ± 0.1	$+1321 \pm 13$	18	53	3.7	5.9	9.2	13
Chromospherically Active Field Stars									
GJ 873	3400, 4.8	4.7 ± 0.1	$+545 \pm 5$	20	115	5.1	7.9	12	16
β Pic Stars									
AU Mic	3800, 4.2	8.7 ± 0.2	-4130 ± 33	14	125	11	17	23	32
AG Tri A	3800, 4.2	4.7 ± 0.1	$+6743 \pm 26$	14	98	10	17	22	33
AG Tri B	3800, 4.2	5.0 ± 0.1	$+5961 \pm 35$	14	132	9.9	14	20	29
GJ 182	3800, 4.2	9.4 ± 0.7	$+19818 \pm 42$	6	103	12	19	25	54
GJ 3305	3800, 4.2	5.7 ± 0.1	$[+20625]$	5	457
GJ 799 A	3800, 4.2	9.6 ± 0.6	-3727 ± 40	14	151	3.9	5.9	8.2	12
GJ 799 B	3200, 4.2	14.7 ± 0.4	-5126 ± 50	13	179	6.0	7.7	12	18
GJ 871.1 A	3200, 4.2	13.9 ± 0.5	$+3087 \pm 36$	14	134	5.7	8.6	12	19
GJ 871.1 B	3200, 4.2	22.7 ± 0.3	$+2031 \pm 44$	15	169	5.2	7.3	10	15
HIP 12545	3800, 4.2	8.7 ± 0.2	$+8253 \pm 48$	14	179	12	17	23	33
TW Hya Stars									
TWA 7	3800, 4.2	4.7 ± 0.1	$+12446 \pm 14$	12	94	7.4	12	19	25
TWA 8A	3600, 4.2	4.7 ± 0.1	$+8679 \pm 23$	15	90	6.7	10	15	22
TWA 8B	3400, 4.2	10.5 ± 0.3	$+8607 \pm 32$	15	123	3.6	4.5	7.1	11
TWA 9A	4000, 4.2	10.4 ± 0.3	$+11649 \pm 21$	11	71	15	25	30	47
TWA 9B	3800, 4.2	8.6 ± 0.3	$+12279 \pm 27$	11	90	8.8	15	20	29
TWA 11B	3600, 4.2	12.0 ± 0.2	$+8923 \pm 59$	11	191	10	12	19	29
TWA 12	3600, 4.2	17.0 ± 0.3	$+12498 \pm 52$	12	181	11	14	20	31
TWA 13A	3800, 4.2	11.1 ± 0.3	$+11668 \pm 65$	14	242
TWA 13B	3600, 4.2	10.7 ± 0.3	$+12075 \pm 43$	13	149	9.0	13	18	26
TWA 23	3800, 4.2	20.5 ± 5.5	$[+6520]$	15	2425

stead of synthetic spectra and/or multiple-Gaussian instrumental profiles. Errors inherent to our modeling prescription are incorporated into the instrument error reported here. Regardless, this precision is considerably better than intended in the design specifications, and a credit to the talent of the instrument team.

Measurement errors are assigned to each observation (listed in the Appendix) by calculating σ_{phot} for each pair-averaged observation, and adding that in quadrature with an assumed constant σ_{inst} of 46 m/s. These errors do not account for any possible errors due to stellar activity (σ_{stel}). The RV errors listed in the Appendix for the 21 young stars range from 46 m/s to 79 m/s with a median values of 53 m/s. The σ_{obs} values are nevertheless significantly larger than these error estimates, ranging from 71 - 197 m/s for the single stars (identified below). This implies a significant contribution from the σ_{stel} to the observed dispersions.

Since stellar activity is known to be correlated with rotational velocity (e.g. Baliunas et al. 1995), we investigate the relation between the observed dispersions and projected rotational velocities in Figure 3. Although there is considerable spread in the dispersion values near a $v \sin i = 10$ km/s, the 2 quantities nevertheless appear to be correlated. Stars with $v \sin i$ values less than 12 km/s have a median dispersion of 115 m/s while those rotating more rapidly have a median dispersion of 179 m/s.

6.2. New and Candidate RV Variables

We use the apparent relation between the observed RV dispersions (σ_{obs}) and $v \sin i$ values illustrated in Figure 3 to objectively identify possible RV variables. To do this, a quadratic polynomial is fit to the data iteratively; stars with dispersions 2σ above the best fit are identified as possible RV variables and subsequently excluded from the fit. This identified 3 stars as possible variable stars, TWA 23, GJ 3305, and TWA 13A. We note that these same stars would be identified using a linear fit to the data, but we adopt and illustrate in Figure 3 a quadratic fit which can account for saturation in the dispersion, if present, given the limited range of dispersions observed (see below).

Two stars have dispersions well above their predicted dispersion for their $v \sin i$, TWA 23 ($\sigma_{obs} = 2425$ m/s) and GJ 3305 ($\sigma_{obs} = 457$ m/s; Table 2). These large dispersions, in combination with their smoothly accelerating RV variations illustrated in Figure 4 confidently indicate that these stars are spectroscopic binaries. In the case of GJ 3305, the observed variations are likely due to its 0'093 companion (Kasper et al. 2007). The discovery of this spatially resolved companion mid-way through our observational program is why we have fewer observations of it; it was considered a less likely place to find a young planet. In the case of TWA 23, the follow-up observations in 2009 helped to establish an upper limit on its orbital period, but its orbit is still underdeter-

mined. In Figure 5 we show 3 plausible orbital solutions for TWA 23, determined using a standard iterative non-linear least-squares method (Levenberg-Marquardt, outlined in Press et al. 1992, p. 650); with rms residuals of ~ 0.2 km/s in all cases, the 3 fits are equally good. The orbital periods of these 3 fits are 517 d, 777 d, and 1552 d with amplitudes of 4 km/s, 5 km/s, and 5 km/s. As with GJ 3305, its companion is more likely to have a stellar mass. Nevertheless, the discovery of these relatively low amplitude spectroscopic binaries highlights the potential for new discoveries that high-precision infrared RVs have when applied to young stars.

The RV dispersion of one other star stands out as being marginally above (3.4σ) the best-fit relation, TWA 13A. Inspection of its RV curve shown in Figure 4 reveals large amplitude variations (> 200 m/s) on relatively short (1-2 day) timescales. These types of variations are the type expected if TWA 13A is orbited by a hot Jupiter-like companion. Unfortunately our sampling and precision are insufficient to confirm this possibility. We classify it as a candidate variable⁴

It is possible that the larger-than-expected RV dispersion of TWA 13A is caused by either instrumental errors or stellar activity being larger than expected for this star during these observations; these sources of variation are harder to predict and account for. As a possible test for the former, we compared the RV dispersion of TWA 13A to that of its companion TWA 13B. Both stars are equally bright ($K = 7.5$) and in 13 of TWA 13A's 14 observations, both stars were observed either immediately before or after one another. If the NIRSPEC detector was especially noisy during these observations, it likely would have affected observations of TWA 13B as well. However, the observed dispersion of TWA 13B ($\sigma_{obs} = 149$ m/s) agrees almost exactly with that predicted from its $v \sin i$ (142 m/s). This strengthens the case that TWA 13A is a RV variable star, but unfortunately it is not yet possible to determine if the variations are caused by a companion or stellar activity.

7. DISCUSSION

7.1. Companion Detection Limits

Companion mass detection limits are determined via Monte Carlo simulations. Since this survey is most sensitive to short period companions, we set limits only at representative orbital periods, namely 3, 10, 30 and 100 days. The shortest period is chosen to be near the peak in the orbital period distribution of hot Jupiters while the other periods are chosen to demonstrate how the sensitivity declines with increasing orbital period, given the precision and temporal sampling of this survey. For each star, a set of 10,000 orbits is generated with random inclinations, phases, and companions spanning a broad range of planetary and brown dwarf masses. For discussion purposes, we refer to companions with masses $\leq 13 M_{Jupiter}$ as planets and more massive companions (up to $\sim 65 M_{Jupiter}$) as brown dwarfs. All orbits are assumed

⁴ Prior to the follow-up observations in 2009, TWA 13A was even further above the best fit relation ($\sigma_{obs} = 261$ m/s versus 242 m/s); the new observations near its mean reduced its overall dispersion. However, since it was initially identified as a candidate variable for follow-up observations, and remains somewhat discrepant with its expected precision, we continue to classify it as a candidate RV variable.

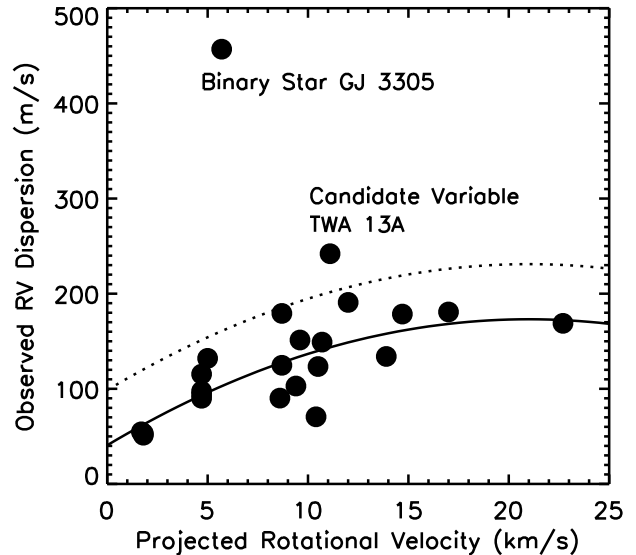


Figure 3. RV dispersion versus projected rotational velocities; with a dispersion of 2425 m/s, TWA 23 is not illustrated on this plot. A quadratic function is fit via least squares to the data (solid line) and systems with dispersions 2σ above this best fit (dotted line) are considered candidate RV variables.

to be circular, as would be expected if these companions migrated to these locations via disk interactions (e.g. Lin et al. 1996). In combination with the stellar masses listed in Table 1, these orbits are used to predict a set of RV measurements with the same temporal sampling as each star's set of observations. An assumed Gaussian error of 53 m/s, equal to the median observational error above ($\sigma_{phot} + \sigma_{inst}$), is added to these measurements; we note however that adding these relatively small errors has no significant effect upon the results. Conservative detection limits are then set by determining the companion mass that induces a RV dispersion that is 2σ greater than the expected dispersion for the star's $v \sin i$ (see Figure 3) 99% of the time; this is consistent with the criteria used to identify candidate variables such as TWA 13A.

The companion detection limits determined from this prescription at 3, 10, 30, and 100 days are listed for all single stars in Table 2. The 3 field stars, which have the smallest RV dispersions, have the lowest companion mass detection limits. On average, these are 4.1, 6.0, 10, and 13 $M_{Jupiter}$ for the above 4 orbital periods, respectively. These observations confirm that these stars have no short-period massive planet or brown dwarf companions at any orbital orientation except possibly nearly face-on.

In assessing the young stars detection limits, we exclude the known or candidate RV variables and use only results for stars with 11 or more observations (thus excluding GJ 182 with only 6 observations). For this 18 star subsample, the average detection limits are 8.5, 13, 17, and 26 $M_{Jupiter}$ at the above 4 orbital periods, respectively. The lowest mass stars within this subset have the lowest companion detection limits, as expected since the detection limit scales as $M_{star}^{2/3}$. For example, the 0.12 M_{\odot} star TWA 8B has the smallest detection limits of 3.6, 4.5, 7.1, and 10.6 $M_{Jupiter}$, respectively, despite

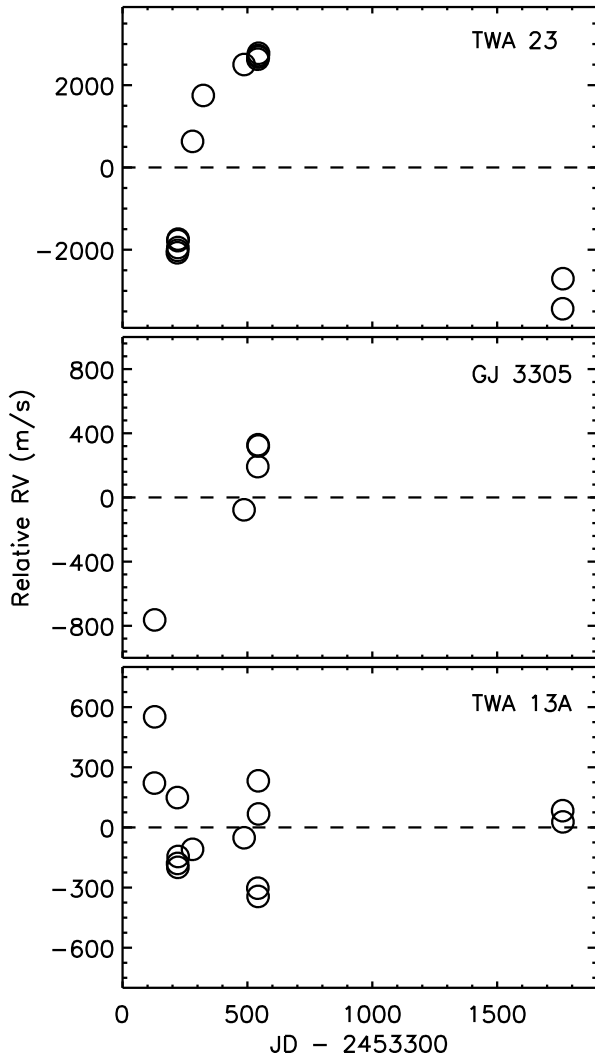


Figure 4. RV curves for the new binary stars TWA 23 and GJ 3305, and the candidate RV variable TWA 13A; typical uncertainties in these measurements are 50-60 m/s. The long time-scale (> 1 yr) RV trends of TWA 23 and GJ 3305 are indicative of low mass stellar, or possibly brown dwarf companions. In the case of GJ 3305, the motion is likely due to its spatially resolved companion (Kasper et al. 2007). The large amplitude, short-timescale variations of TWA 13A are indicative of a short-period gas giant planet (e.g. a hot Jupiter), but the data are insufficient to confirm this.

having an observed dispersion of 123 m/s. Overall, the observations only exclude the presence of the very massive hot ($P < 10$ d) Jupiters. However, the observations confidently exclude all hot brown dwarf companions and all but the lowest mass ‘warm’ ($10 < P < 100$ d) brown dwarf companions.

The RV measurements would translate to much stricter companion detection limits if the companion’s orbital plane is assumed to be edge-on. This assumption is plausible for the young star AU Mic that is known to harbor an edge-on circumstellar disk (e.g. Kalas et al. 2004). At an assumed age of 12 Myr, its M0 spectral type corresponds to a stellar mass of $0.73 M_{\odot}$. For this star, we calculate companion detection limits using the same Monte Carlo simulations described above, but assuming

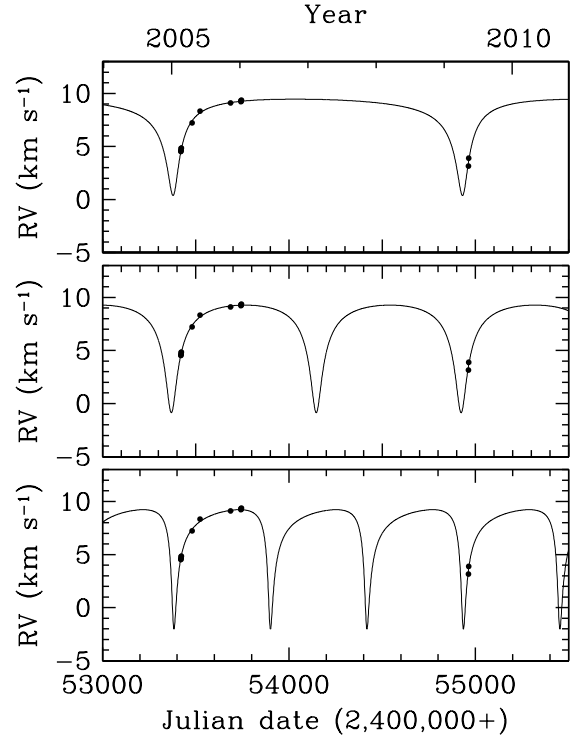


Figure 5. Three plausible orbits for the binary star TWA 23, with periods of 1552 d, 777 d, and 517 d.

an edge-on orientation for the orbit. This yields companion detection limits of 1.8, 2.5, 3.9 and 5.2 $M_{Jupiter}$ at the above 4 periods, respectively. These detection limits are consistent with the lack of any transiting Jupiter-sized planets found in this system (Hebb et al. 2007). If massive Jupiters do exist within the AU Mic system, they have not migrated inwards in its ~ 12 Myr lifetime.

7.2. The Effect of Stellar Activity on Precision RV Measurements

One of the primary motivations for conducting this RV survey of young stars at infrared wavelengths, as opposed to optical wavelengths, was to mitigate the RV variations induced by stellar activity; we subsequently refer to this as stellar jitter. To investigate the success of this, we compare estimates of the stellar jitter of our infrared observations to the estimates from optical observations. The infrared stellar jitter is estimated by subtracting, in quadrature, the instrumental and average theoretical errors from the observed dispersion for each star ($\sigma_{stel}^2 = \sigma_{obs}^2 - \sigma_{inst}^2 - \sigma_{phot}^2$). This yielded values ranging from 36 m/s to 181 m/s, with a median value of 113 m/s; these are illustrated in Figure 6 versus $v \sin i$.

The values are then compared to the stellar jitter values calculated from RV measurements in Paulson & Yelda (2006), who obtained precise optical RV measurements of 6 members of the β Pic Association, including 2 stars in the present survey here, AU Mic and GJ 3305. GJ 3305 is not included in these comparisons, however, because we identify it as a spectroscopic binary star. Paulson & Yelda (2006) obtained precise RVs using the telluric oxygen band at 6900 Å with an instrumental precision of 40 m/s. As with the infrared measurements, the stellar jitter is estimated by subtracting, in quadrature, the theoretical and instru-

mental uncertainties from the observed velocity dispersions. These results are plotted in Figure 6 versus $v \sin i$, and range from 270 m/s to 490 m/s, with a mean of 360 m/s. A comparison of these suggests that the stellar jitter at infrared (K -band) is approximately 3 times less than at optical wavelengths (R -band). This is consistent with the reductions measured by Huélamo et al. (2008) for the similar age star TW Hya. The recent study by Mahmud et al. (2011) reports similar reductions between infrared and optical jitter for the younger T Tauri stars DN Tau and Hubble I 4, and slightly larger reductions (a factor 4-5) for V827 Tau and V836 Tau.

Although the binary star GJ 3305 is not included in these comparisons, we note that Paulson & Yelda (2006) do not identify it as a spectroscopic binary, despite having observed it 11 times on 4 different nights. We attribute this to their limited sampling, its apparently low amplitude RV variations, and the larger stellar jitter associated with optical observations of young stars. We also note that we can not confirm the claim of Song et al. (2003) that HIP 12545 is a single-lined spectroscopic binary. Although they do not report individual measurements, they claim to have measured large (20 km/s) RV variations for this star using on high dispersion optical spectra. Our 14 measurements of this star spanning from 2004 November 19 to 2006 July 6 have a dispersion of only 0.18 km/s.

Altogether these results confirm the expectation that infrared observations mitigate the RV variations due to stellar activity and, moreover, quantify the benefit. As discussed in the introduction, this is expected if the RV variations are primarily caused by cool star spots. However, infrared observations made during other chromospheric events such as giant flares or coronal mass ejections may have little or no benefit over optical measurements. It has been shown that giant flares on active stars can cause temporary shifts in optically determined RV of several hundred m/s (Reiners 2009). Although we do not have information to identify flare or flare-like events in our data, this could explain the occasional large (> 200 m/s), one-time RV changes seen for some stars. One of our clearest examples occurred during observations of the slowly rotating star TWA 7 ($v \sin i = 4.5$ km/s). As illustrated in Figure 7, all but 1 of its 12 RV measurements are consistent to within 100 m/s ($\sigma_{\text{obs}} = 47$ m/s); the discrepant epoch deviates by ~ 300 m/s from the mean RV of the other 11 epochs. Comparisons of stars observed immediately before and after this epoch show no similar large amplitude deviations, which might be expected if the detector was especially noisy at this time; the deviation appears to be limited to this observation. The SNR of this observation is also above the mean of the remaining observations, and the spectrum shows no defects, such as an cosmic ray event that was not corrected in the optimal extraction. This leads us to believe the deviation is intrinsic to the star itself. Because we can't fully explain the event (or others like it), we highlight it here as a cautionary remark for future surveys. Coordinated photometric and/or spectroscopic observations that target chromospheric indicators may help identify these events, which when excluded, would improve the overall sensitivity to low mass companions.

Finally, the ensemble infrared stellar jitter results provide a guide for the achievable RV precision for young

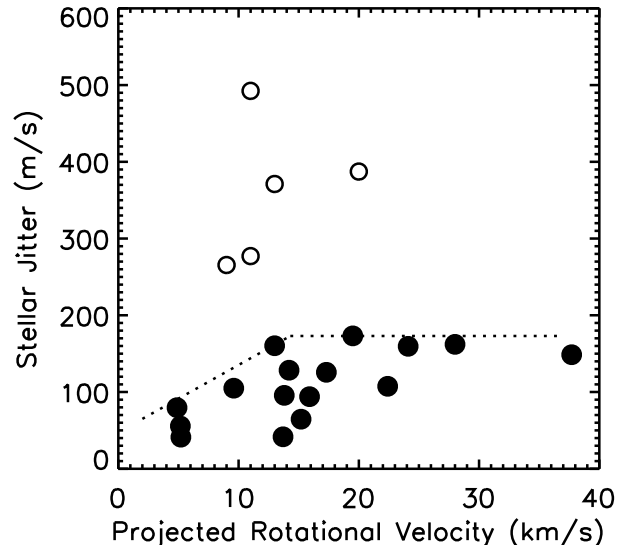


Figure 6. Stellar jitter versus projected rotational velocity. The stellar jitter at infrared wavelengths (*solid circles*) is significantly less than at optical wavelengths (*empty circles*), as expected if it is primarily caused by cool star spots. The *dotted line* illustrates the upper boundary of infrared stellar jitter values, and illustrates the tentative evidence for saturation at ~ 180 m/s for $v \sin i$ values above 12 km/s.

active stars in the limit of high SNR spectra with no wavelength calibration error. For the slowest rotating stars ($v \sin i < 6$ km/s), the median stellar jitter is 77 m/s (1 σ spread of 21 m/s). For stars with modest rotation ($6 \text{ km/s} < v \sin i < 12 \text{ km/s}$), the median stellar jitter is 108 m/s (1 σ spread of 43 m/s). And for the most rapidly rotating stars ($v \sin i$ of 12 - 23 km/s), the median stellar jitter is 168 m/s (1 σ spread of 24 m/s). We also note that none of the 4 stars with $v \sin i$ values > 12 km/s have stellar jitter values above 180 m/s, possibly hinting at stellar jitter saturation (Figure 6). Although the available data cannot robustly confirm this, we highlight this possibility because this $v \sin i$ limit is similar to the observed X-ray saturation limit of ~ 15 km/s, though for slightly more massive stars in the Pleiades (Stauffer et al. 1994); the X-ray saturation is interpreted as a consequence of maximal coverage of star spots. Likewise, we find that stars with the largest stellar jitter have rotational periods < 3.3 days (Table 1). As demonstrated in (Pizzolato et al. 2003), subsolar mass stars with rotation periods $< 3.0 - 3.5$ days (depending somewhat on mass) all have saturated X-ray emission. Given that the most rapidly rotating stars studied here appear to be near or beyond the regime where X-rays saturate, its plausible to presume that the stellar jitter is also saturated. The results have implications for how precisely the radial velocities of rapidly rotating stars can be determined.

8. SUMMARY

We present the results of a high-precision infrared RV study of 20 young stars in the β Pic and TW Hya Associations, as well as the chromospherically active, young disk M3.5 star GJ 873. High spectral resolution ($R \sim 30,000$) measurements at $2.3 \mu\text{m}$ were obtained with

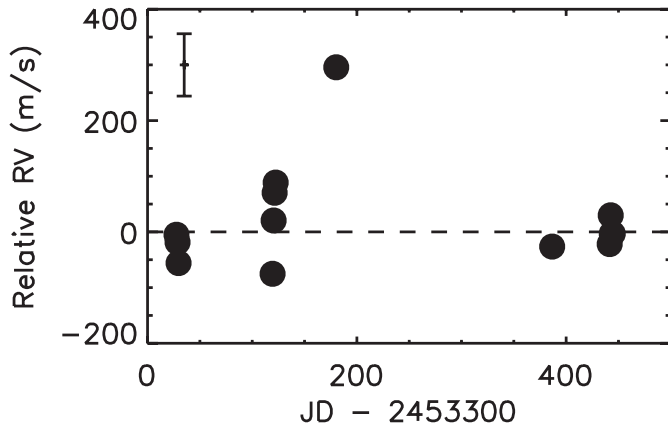


Figure 7. RV curve of the slowly rotating young star TWA 7; an average errorbar is illustrated in the upper left. All but 1 of the RVs are consistent to within 100 m/s ($\sigma = 47$). The one outlier is possibly due to a transient stellar event such as a flare.

NIRSPEC at the Keck Observatory; the majority of stars have more than a dozen epochs, with a typical temporal sampling of several observations over a week-long run, and then several runs over 2 to 3 years. Precise RVs are determined using telluric absorption features as an absolute wavelength reference. Each observation is modeled as the combination of a telluric spectrum and a synthetically generated stellar spectrum, both convolved by a parametrized instrumental profile and projected onto a parametrized wavelength solution. The best fit, which includes the RV of the star, is determined by minimizing the χ^2 .

This modeling technique yields RV dispersions of ~ 50 m/s for 13+ epochs each of 3 slowly rotating field stars. The dispersion of these RV measurements is dominated by instrumental errors and thus ~ 50 m/s can be considered a practical precision limit for NIRSPEC (see also Blake et al. 2010); this precision is nevertheless well above NIRSPEC’s original design specifications. Significant improvements to this precision will likely require a new detector to mitigate dominant noise sources such as fringing, variable bias, and read noise.

The observed RV dispersions for young stars range from 48 m/s to 197 m/s. These dispersions are dominated by noise from stellar activity, or stellar jitter. We estimate the contribution from stellar jitter by subtracting, in quadrature, the average instrumental noise (46 m/s) and the calculated theoretical noise (~ 40 m/s) from the observed dispersions. The stellar jitter increases with projected rotational velocity ($v \sin i$). The slowest rotating stars ($v \sin i < 6$ km/s) have a median stellar jitter of 77 m/s, modest rotation stars ($6 \text{ km/s} < v \sin i < 12$ km/s) have a median stellar jitter of 108 m/s, and the most rapidly rotating stars ($v \sin i$ of 12 - 23 km/s) have a median stellar jitter of 168 m/s. There is also tentative evidence that stellar jitter saturates at ~ 180 m/s above $v \sin i$ values of ~ 12 km/s, or below rotational periods of $\sim 3 - 4$ days, consistent with the rate of rotation that causes X-rays to saturate.

These infrared stellar jitter values are, on average, a factor of 3 less than the stellar jitter values of similar age β Pic Association stars observed at optical (R-band) wavelengths. Case studies by Huélamo et al. (2008) and Mahmud et al. (2011) corroborate these reductions. This is expected if stellar jitter is predominantly caused

by cool star spots, and confirms that infrared measurements have a significant advantage over optical measurements in obtaining precise RV measurements of active stars.

Three stars have RV dispersions significantly above the level expected for their $v \sin i$. The smoothly accelerating RVs of 2 of these stars, GJ3305 and TWA 23, indicate they are single-lined spectroscopic binaries. The RV orbits are still under-determined. In the case of GJ 3305, the motion is likely caused by its recently identified ~ 93 milliarcsecond companion (Kasper et al. 2007). The 3rd star, TWA 13A, exhibits large amplitude (> 200 m/s), short-timescale variations indicative of a hot Jupiter-like companion, but the available data are insufficient to confirm this. We label it as a candidate RV variable. We also note that the relative rarity of hot Jupiter companions ($\sim 1\%$) implies that a first discovery in this small sample of 20 young stars would be most fortuitous.

For the remainder of the sample, these observations exclude the presence of any ‘hot’ ($P < 3$ days) companions more massive than $8 M_{Jup}$, and any ‘warm’ ($P < 30$ day) companions more massive than $17 M_{Jup}$, on average. Assuming an edge-on orbit for the edge-on disk system AU Mic, these observations exclude the presence of any hot Jupiters more massive than $1.8 M_{Jup}$ or warm Jupiters more massive than $3.9 M_{Jup}$. If massive Jupiters exist in the AU Mic system, they have not migrated inwards in its ~ 12 Myr lifetime.

While the effect of star spots will continue to be a limiting factor in the search for young short-period planets, even at infrared wavelengths, the results presented here elucidate better the opportunities for determining precise RVs from infrared observations in the limit of high stellar activity.

We are grateful to the support staff at Keck observatory, especially Grant Hill and Jim Lyke, and to the scientists who built and continue to maintain NIRSPEC, especially Dr. Ian McLean. We appreciate the data provided by the NASA/IPAC Infrared Science Archive and the privilege to observe on the revered summit of Mauna Kea.

REFERENCES

- Abranin, E. P., et al. 1998, *A&ApT*, 17, 221
- Adams, F. C. & Laughlin, G. 2003, 2003, 163, 290
- Alibert, Y., Mordasini, C., Benz, W. & Winisdoerffer, C. *A&A*, 434, 343
- Baliunas, S. L., et al. 1995, *ApJ*, 438, 269
- Baraffe, I., Charbrier, G., Allard, F. & Hauschildt, P. H. 1998, *A&A*, 337, 403
- Bean, J. L., Seifahrt, A., Hartmann, H., Nilsson, H., Wiedemann, G., Reiners, A., Dreizler, S. & Henry, T. J. 2010, *ApJ*, 713, 410
- Blake, C., Charbonneau, D., White, R. J., Marley, M. S. & Saumon, D. 2007, *ApJ*, 666, 1198
- Blake, C., Charbonneau, D. & White, R. J. 2010, *ApJ*, 723, 684
- Boss, A. P. 1997, *Science*, 276, 1836
- Boss, A. P. 2004, *ApJ*, 610, 456
- Boss, A. P. 2006, *ApJ*, 644, 79
- Briceño, C., et al. 2001, *Science*, 291, 93
- Butler, R. P. et al. 2006, *PASP*, 118, 1685
- Butler, R. P., Marcy, G. W., Williams, E., McCarthy, C., Dosanjh, P. & Vogt, S. S. 1996, *PASP*, 108, 500
- Carpenter, J. M., Mamajek, E. E., Hillenbrand, L. A., Meyer, M. R. 2006, *ApJ*, 651, 49
- Cochran, W. D. 1988, *ApJ*, 334, 349

- Cochran, W. D., Hatzes, A. P., Butler, R. P. & Marcy, G. W. 1997, *ApJ*, 483, 457
- Crockett, C. J., Mahmud, N. I., Prato, L., Johns-Krull, C. M., Jaffe, D. T. & Beichman, C. A. 2011, *ApJ*, in press
- Cumming, A., Butler, R. P., Marcy, G. W., Vogt, S. S., Wright, J. T. & Fischer, D. A. 2008, *PASP*, 120, 531
- Deming, D., Brown, T. M., Charbonneau, D., Harrington, J. & Richardson, L. J. 2005, *ApJ*, 622, 1149
- Endl, M., Cochran, W. D., Tull, R. G. & MacQueen, P. J. 2006, *AJ*, 132, 2755
- Figueira, P., Marmier, M., Bonfils, X., di Folco, E., Udry, S., Santos, N. C., Lovis, C., Mégevand, D., Melo, C. H. F. & Pepe, F. 2010, *A&A*, 513, 8
- Fischer, D. A., et al. 2006, *ApJ*, 637, 1094
- Feigelson, E. D., Lawson, W. A., Stark, M., Townsley, L. & Garmire, G. P.
- Goldreich, P. & Tremaine, S. 1980, *ApJ*, 241, 425
- Haisch, K., Lada, E. A. & Lada, C. J. 2001, *ApJ*, 553, 153
- Hauschildt, P. H., Allard, F. & Baron, E. 1999, *ApJ*, 512, 377
- Hawley, S. L., Gizis, J. E. & Reid, I. N. 1996, *AJ*, 112, 2799
- Hebb, L. et al. 2007, *MNRAS*, 379, 63
- Henry, T. J., Kirkpatrick, J. D. & Simons, D. A. 1994, *AJ*, 108, 1437
- Henry, T. J. & McCarthy, D. W., Jr. 1993, *AJ*, 106, 773
- Herbst, W., Herbst, D. K., Grossman, E. J., Weinstein, D. 1994, *AJ*, 108, 1906
- Hernán-Obispo, M., Gálvez-Ortiz, M. C., Anglada-Escudé, G., Kane, S. R., Barnes, J. R., de Castro, E. & Cornide, M. 2010, *A&A*, 512, 45
- Hillenbrand, L. A. & White, R. J. 2004, *ApJ*, 604, 741
- Huélamo, N., et al. 2008, *A&A*, 489, 9
- Huerta, M., Johns-Krull, C. M., Prato, L., Hartigan, P. & Jaffe, D. T. 2008, *ApJ*, 678, 472
- Hünsch, M., Schmitt, J. H. M. M., Sterzik, M. F. & Voges, W. 1999, *A&AS*, 135, 319
- Horne, K. 1986, *PASP*, 98, 609
- Howard, A. W., Marcy, G. W., Johnson, J. A., Fischer, D. A., Wright, J. T., Howard, I., Valenti, J. A., Anderson, J., Lin, D. N. C. & Shigeru, I. 2010, *Science*, 330, 653
- Ireland, M. J., Kraus, A., Martinache, F., Law, N. & Hillenbrand, L. A. 2011, *ApJ*, 726, 113
- Johns-Krull, C. M. & Valenti, J. A. 1996, *ApJ*, 459, L95
- Jones, H. R. A., Butler, R. P., Tinney, C. G., Marcy, G. W., Carter, B. D., Penny, A. J., McCarthy, C. & Bailey, J. 2006, *MNRAS*, 369, 249
- Lagrange, A. -M., Bonnefoy, M., Chauvin, G., Apai, D., Ehrenreich, D., Boccaletti, A., Gratadour, D., Rouan, D., Mouillet, D., Lacour, S. & Kasper, M. 2010, *Sci*, 329, 57
- Latham, D. W., Stefanik, R. P., Mazeh, T., Mayor, M. & Burki, G. 1989, *Natur*, 339, 38
- Livingston, W., & Wallace, L. 1991, *Atlas of the Solar Spectrum in the Infrared from 1850 to 9000 cm⁻¹* (NSO Tech. Rep.; Tucson: NSO)
- Leggett, S. 1992, *ApJS*, 82, 351
- Lubow, S. H. & Ida, S. 2010, in *Exoplanets*, edited by S. Seager, Tucson, AZ: University of Arizona Press, p. 347-371
- Kalas, P., Liu, M. C., Matthews, B. C. 2004, *Science*, 303, 1990
- Kalas, P., Graham, J. R., Chiang, E., Fitzgerald, M. P., Clampin, M., Kite, E. S., Stapelfeldt, K., Marois, C. & Krist, J. 2008, *Science*, 322, 1345
- Kasper, M., Apai, D., Janson, M. & Brandner, W. 2007, *A&A*, 472, 321
- Kataria, T. & Simon, M. 2010, *AJ*, 140, 206
- Kraus, A. L. & Hillenbrand, L. A. 2007, *AJ*, 134, 2340
- Nidever, D. L., Marcy, G. W., Butler, R. P., Fischer, D. A., & Vogt, S. S. 2002, *ApJS*, 141, 503
- Kennedy, G. M. & Kenyon, S. J. 2008, *ApJ*, 673, 502
- Lin, D. N. C., Bodenheimer, P. & Richardson, D. C. 1996, *Nature*, 380, 606
- Luhman, K. 2003, *ApJ*, 593, 1093
- Macintosh, B. A., et al. 2008, *SPIE*, 7015, 180
- Mahmud, N., Crockett, C. J., Johns-Krull, C. M., Prato, L., Hartigan, P. M., Jaffe, D. T. & Beichman, C. A. 2011, *ApJ*, in press
- Malmberg, D. & Davies, M. B. 2009, *MNRAS*, 394, 26
- Malmberg, D., de Angeli, F., Davies, M. B., Church, R. P., Mackey, D. & Wilkinson, M. I. 2007, *MNRAS*, 378, 1207
- Marchi, S., Ortolani, S., Nagasawa, M. & Ida, S. 2009, *MNRAS*, 394, 93
- Marcy, G. W. & Butler, R. P. 1996, *ApJ*, 464, 147
- Marois, C., Macintosh, B., Barman, T., Zuckerman, B., Song, I., Patience, J., Lafrenière, D. & Doyon, R. 2008, *Science*, 322, 1348
- Mathieu, R. D., Baraffe, I., Simon, M., Stassun, K. G. & White, R. J. 2007, *Protostars and Planets V*, B. Reipurth, D. Jewitt, and K. Keil (eds.), University of Arizona Press, Tucson, 951 pp., 2007., p.411-425
- Mayer, L., Quinn, T., Wadsley, J. & Stadel, J. 2002, *Science*, 298, 1756
- Mayor, M. & Queloz, D. 1995, *Nature*, 378, 355
- Meru, F. & Bate, M. R. 2010, *MNRAS*, 406, 2279
- Meru, F. & Bate, M. R. 2011, *MNRAS*, 411, 1
- Messina, S., Desidera, S., Turatto, M., Lanzafame, A. C. & Guinan, E. F. 2010, *A&A*, 520, 15
- McLean, I. S., et al. 1998, *Proc. SPIE*, 3354, 566
- Mentuch, E., Brandeker, A., van Kerkwijk, M. H., Jayawardhana, R. & Hauschildt, P. H. 2008, *ApJ*, 689, 1127
- Mizuno, H. 1980, *PThPh*, 64, 544
- Muirhead, P. S., et al. 2011, *PASP*, in press.
- Nelder, J. A. & Mead, R. 1965, *Computer Journal*, 7, 308
- Neuhäuser, R., Guenther, E. W., Wuchterl, G., Maugrauer, M., Bedalov, A. & Hauschildt, P. H. 2005, *A&A*, 435, 13
- Osten, R. A., Hawley, S. L., Allred, J., Johns-Krull, C. M., Brown, A. & Harper, G. M. 2006, *ApJ*, 647, 1349
- Pascucci, I., et al. 2006, *ApJ*, 651, 1177
- Paulson, D. B. & Yelda, S. 2006, *PASP*, 118, 706
- Pettersen, B. R., Evans, D. S., Coleman, L. A. 1984, 282, 214
- Piskunov, N., E. & Valenti, J. A. 2002, *A&A*, 385, 1095
- Pizzolato, N., Maggio, A., Micela, G., Sciortino, S. & Ventura, P. 2003, *A&A*, 397, 147
- Pollack, J. B., Hubickyj, O., Bodenheimer, P., Lissauer, J. J., Podolak, M. & Greenzweig, Y. 1996, *Icarus*, 124, 62
- Pont, F., et al. 2009, *A&A*, 502, 695
- Prato, L., Huerta, M., Johns-Krull, C. M., Mahmud, N., Jaffe, D. T. & Hartigan, P. 2008, *ApJ*, 687, 103
- Press, W. H., Teulolsky, S. A., Vetterling, W. T. & Flannery, B. P. 1992, *Numerical Recipes in C. The Art of Scientific Computing*, Cambridge: University Press, 1992, 2nd ed.
- Queloz, D., Henry, G. W., Sivan, J. P., Baliunas, S. L., Beuzit, J. L., Donahue, R. A., Mayor, M., Naef, D., Perrier, C. & Udry, S. 2001, *A&A*, 379, 279
- Raymond, S. N., et al. 2011, *A&A*, 530, 62
- Reiners, A. & Basri, G. 2007, *AJ*, 656, 1121
- Reiners, A. 2009, *A&A*, 498, 853
- Reiners, A., Bean, J. L., Huber, K. F., Dreizler, S., Seifahrt, A. & Czesla, S. 2010, *ApJ*, 710, 432
- Robinson, S. E., Laughlin, G., Bodenheimer, P. & Fischer, D. 2006, *ApJ*, 643, 484
- Saar, S. H. & Donahue, R. A. 1997, *ApJ*, 485, 319
- Sato, B., et al. 2005, *ApJ*, 633, 465
- Santos, N. C., Benz, W. & Mayor, M. 2005, *Science*, 310, 251
- Seifahrt, A. & Käufel, H. U. 2008, *A&A*, 491, 929
- Seifahrt, A., Käufel, H. U., Zängl, G., Bean, J. L., Richter, M. J. & Siebenmorgen, R. 2010, *A&A*, 524, 11
- Setiawan, J., Henning, Th., Launhardt, R., Müller, A., Weise, P., Kürster, M. 2008, *Nature*, 451, 38
- Setiawan, J., Weise, P., Henning, Th., Launhardt, R., Müller, A. & Rodmann, J.
- Siess, L., Dufour, E. & Forestini, M. 2000, *A&A*, 358, 593
- Song, I., Zuckerman, B. & Bessell, M. S. 2003, *ApJ*, 599, 342
- Song, I., Bessell, M. S. & Zuckerman, B. 2003, *ApJ*, 581, 43
- Stauffer, J. R., Caillault, J.-P., Gagné, M., Prosser, C. F. & Hartmann, L. W. 1994, *ApJS*, 91, 625
- Sterzik, M. F., Alcalá, J. M., Covino, E. & Petr, M. G. 1999, *A&A*, 346, 41
- Tamuz, O. et al. 2008, *A&A*, 480, 33
- Torres, c. A. O., Quast, G. R., Melo, C. H. F. & Sterzik, M. F. 2008, in 'Handbook of Star Forming Regions, Volume II: The Southern Sky', p. 757, ASP Monograph Publications, ed. B. Reipurth,
- Udry, S. & Santos, N., C. 2007, *ARA&A*, 45, 397
- Walker, G. A. H., Walker, A. R., Irwin, A. W., Larson, A. M., Yang, S. L. S. & Richardson, D. C. 1995, *Icarus*, 116, 359

- Webb, R. A., Zuckerman, B., Platais, I., Patience, J., White, R. J., Schwartz, M., J. & McCarthy, C. 1999, ApJ, 512, 63
- Wright, J. T., Fakhouri, O., Marcy, G. W., Eunhyu, H., Ying, F., Johnson, J. A., Howard, A. W., Fischer, D. A., Valenti, J. A., Anderson, J. & Piskunov, N. 2010, PASP, in print
- Zuckerman, B. & Song, I. 2004, ARA&A, 42, 685

APPENDIX

INDIVIDUAL RADIAL VELOCITY MEASUREMENTS

Below are the individual RV measurements for the 24 stars observed in this survey. The first column provides the star name, the number of RV measurements, the mean radial velocity its uncertainty, and the standard deviation of RV measurements. The Julian Dates of the observation are listed in the 2nd column and the barycentric RVs and associated uncertainties are listed in the 3rd column.

Table 3
Observational Sample

Star	HJD - 2,400,000	Radial Velocity (m/s)	SNR
GJ 628 N=13 $\bar{RV} = -21,113 \pm 15$ $\sigma = 54.84$	53522.337	-21,061 \pm 51	141
	53523.502	-21,077 \pm 52	203
	53597.224	-21,139 \pm 53	183
	53741.688	-21,104 \pm 57	141
	53742.688	-21,140 \pm 52	198
	53743.685	-21,145 \pm 46	264
	53929.374	-21,084 \pm 53	221
	53930.307	-21,028 \pm 53	147
	53931.387	-21,123 \pm 53	205
	54308.353	-21,251 \pm 53	208
	54309.355	-21,145 \pm 49	278
	54311.343	-21,095 \pm 51	214
	54312.274	-21,083 \pm 51	241
GJ 725A N=18 $\bar{RV} = -611 \pm 12$ $\sigma = 51.24$	53419.683	-557 \pm 57	161
	53420.687	-587 \pm 54	186
	53421.580	-553 \pm 51	221
	53422.638	-647 \pm 51	230
	53522.547	-627 \pm 53	187
	53523.419	-546 \pm 54	191
	53523.618	-608 \pm 50	261
	53596.363	-543 \pm 53	191
	53597.343	-703 \pm 50	248
	53670.202	-707 \pm 47	206
	53928.535	-578 \pm 50	275
	53929.453	-631 \pm 51	260
	53930.410	-623 \pm 59	147
	53931.463	-614 \pm 52	173
	54308.364	-636 \pm 54	198
	54309.399	-561 \pm 55	172
	54311.377	-680 \pm 54	176
	54312.291	-605 \pm 53	196
GJ 725B N=18 $\bar{RV} = 1,321 \pm 13$ $\sigma = 53.07$	53419.682	1,305 \pm 55	178
	53420.686	1,319 \pm 59	144
	53421.578	1,352 \pm 52	150
	53422.636	1,329 \pm 50	261
	53522.549	1,410 \pm 52	194
	53523.421	1,411 \pm 51	233
	53523.621	1,329 \pm 52	233
	53596.365	1,376 \pm 53	196
	53597.344	1,278 \pm 54	183
	53670.204	1,388 \pm 47	151
	53928.538	1,324 \pm 52	241
	53929.455	1,266 \pm 55	200
	53930.412	1,282 \pm 54	194
	53931.489	1,347 \pm 53	205
	54308.367	1,278 \pm 57	172
	54309.401	1,226 \pm 55	172
	54311.379	1,253 \pm 53	206
	54312.293	1,304 \pm 52	218
GJ 182 N=6 $\bar{RV} = 19,818 \pm 42$ $\sigma = 102.91$	53327.568	19,753 \pm 53	172
	53328.596	19,732 \pm 55	184
	53686.442	19,696 \pm 52	166
	53741.468	19,941 \pm 50	224
	53742.409	19,898 \pm 56	175
	53743.389	19,887 \pm 57	176
GJ 873 N=21 $\bar{RV} = 545 \pm 25$ $\sigma = 112.93$	53327.225	606 \pm 62	142
	53328.198	656 \pm 47	141
	53522.592	502 \pm 58	147
	53523.587	418 \pm 55	136
	53596.442	559 \pm 55	175
	53597.401	547 \pm 54	165
	53669.328	303 \pm 56	136

Table 3 — *Continued*

Star	HJD - 2,400,000	Radial Velocity (m/s)	SNR
	53670.352	442 \pm 54	179
	53686.247	558 \pm 52	198
	53742.205	710 \pm 55	167
	53743.187	719 \pm 58	150
	53744.187	780 \pm 48	128
	53928.569	469 \pm 57	179
	53929.516	525 \pm 51	215
	53929.615	476 \pm 48	383
	53930.538	385 \pm 55	170
	53931.493	542 \pm 49	160
	54308.411	589 \pm 57	149
	54309.429	565 \pm 53	152
	54311.430	554 \pm 57	164
	54312.359	541 \pm 52	201
AU Mic	53522.559	-4,083 \pm 54	181
N=14	53523.549	-4,151 \pm 54	193
$\bar{RV} = -4,130 \pm 33$	53596.369	-4,020 \pm 52	206
$\sigma = 124.74$	53597.379	-4,112 \pm 51	228
	53669.193	-4,018 \pm 52	205
	53670.196	-3,869 \pm 47	212
	53928.504	-4,206 \pm 49	336
	53929.448	-4,280 \pm 50	274
	53930.456	-4,225 \pm 54	187
	53931.396	-4,156 \pm 50	248
	54308.426	-4,008 \pm 53	211
	54309.411	-4,298 \pm 50	284
	54311.404	-4,111 \pm 54	195
	54312.356	-4,289 \pm 52	205
AG Tri A	53327.386	6,692 \pm 53	208
N=14	53328.376	6,650 \pm 57	163
$\bar{RV} = 6,743 \pm 26$	53329.442	6,650 \pm 56	151
$\sigma = 97.53$	53421.202	6,780 \pm 53	196
	53422.198	6,766 \pm 53	198
	53669.334	6,759 \pm 50	228
	53670.356	6,723 \pm 51	226
	53686.257	6,552 \pm 53	163
	53686.512	6,620 \pm 57	140
	53742.259	6,830 \pm 56	200
	53744.196	6,878 \pm 48	149
	53928.604	6,830 \pm 64	123
	53929.591	6,824 \pm 52	223
	53930.583	6,840 \pm 52	213
AG Tri B	53327.389	5,845 \pm 51	260
N=14	53328.378	5,939 \pm 53	212
$\bar{RV} = 5,961 \pm 35$	53329.445	6,124 \pm 60	126
$\sigma = 132.05$	53421.204	6,126 \pm 54	193
	53422.201	5,920 \pm 52	221
	53669.336	5,888 \pm 50	252
	53670.359	5,699 \pm 51	231
	53686.259	5,871 \pm 52	192
	53686.514	5,843 \pm 52	210
	53742.262	6,147 \pm 56	240
	53744.198	6,073 \pm 48	167
	53928.609	6,075 \pm 68	116
	53929.597	5,981 \pm 50	271
	53930.587	5,923 \pm 52	227
GJ 3305	53328.592	19,862 \pm 52	209
N=5	53686.440	20,548 \pm 58	159
$\bar{RV} = 20,625 \pm 204$	53741.455	20,817 \pm 52	174
$\sigma = 457.20$	53742.407	20,954 \pm 51	242
	53743.387	20,946 \pm 52	237
GJ 799 A	53522.564	-3,614 \pm 55	175
N=14	53523.539	-3,670 \pm 53	129
$\bar{RV} = -3,727 \pm 40$	53596.372	-3,902 \pm 49	273
$\sigma = 151.32$	53597.381	-4,055 \pm 51	218
	53669.188	-3,556 \pm 57	151
	53670.193	-3,572 \pm 47	204
	53928.490	-3,911 \pm 50	207
	53929.439	-3,722 \pm 54	193
	53930.450	-3,658 \pm 52	164
	53931.391	-3,621 \pm 49	294
	54308.357	-3,749 \pm 53	203
	54309.406	-3,850 \pm 54	185
	54311.400	-3,727 \pm 53	196
	54312.351	-3,570 \pm 52	204

Table 3 — *Continued*

Star	HJD - 2,400,000	Radial Velocity (m/s)	SNR
GJ 799 B	53522.561	-4,946 \pm 55	160
N=14	53523.547	-5,358 \pm 60	181
$\bar{RV} = -5,126 \pm 55$	53596.374	-5,165 \pm 53	253
$\sigma = 206.52$	53597.383	-4,726 \pm 49	195
	53669.190	-5,020 \pm 57	195
	53670.190	-4,888 \pm 49	173
	53928.495	-4,969 \pm 52	235
	53929.445	-5,071 \pm 56	216
	53930.454	-5,310 \pm 59	181
	53931.394	-5,198 \pm 54	227
	54308.360	-5,091 \pm 58	193
	54309.408	-5,326 \pm 55	217
	54311.402	-5,477 \pm 60	179
	54312.353	-5,217 \pm 55	211
GJ 871.1 A	53327.203	3,025 \pm 80	151
N=14	53328.183	3,082 \pm 55	181
$\bar{RV} = 3,087 \pm 36$	53329.187	3,185 \pm 55	107
$\sigma = 134.03$	53522.582	3,036 \pm 51	279
	53523.604	2,831 \pm 60	165
	53596.432	3,099 \pm 51	290
	53597.394	3,270 \pm 55	202
	53669.269	3,054 \pm 53	250
	53686.232	3,294 \pm 49	146
	53928.518	3,103 \pm 56	162
	53929.523	3,266 \pm 57	209
	53930.529	3,090 \pm 56	205
	54311.415	2,953 \pm 52	267
	54312.414	2,931 \pm 51	274
GJ 871.1 B	53327.211	2,151 \pm 63	244
N=15	53328.188	2,031 \pm 65	229
$\bar{RV} = 2,031 \pm 44$	53329.195	2,311 \pm 76	170
$\sigma = 168.83$	53522.587	1,872 \pm 62	228
	53523.609	1,834 \pm 71	187
	53596.436	2,125 \pm 65	203
	53597.397	2,017 \pm 68	189
	53669.272	1,722 \pm 79	151
	53686.236	2,298 \pm 50	181
	53928.525	2,069 \pm 61	242
	53930.532	2,164 \pm 66	204
	54308.428	2,056 \pm 77	160
	54309.422	2,053 \pm 58	277
	54311.419	1,923 \pm 59	264
	54312.418	1,846 \pm 58	277
HIP 12545	53328.384	8,407 \pm 54	219
N=14	53329.401	8,399 \pm 73	100
$\bar{RV} = 8,253 \pm 48$	53421.208	8,422 \pm 60	152
$\sigma = 179.25$	53422.205	8,201 \pm 54	202
	53669.402	7,945 \pm 55	193
	53670.393	8,145 \pm 54	195
	53686.263	8,219 \pm 55	166
	53686.519	8,077 \pm 54	182
	53742.255	8,438 \pm 62	160
	53744.203	8,495 \pm 48	140
	53928.614	7,985 \pm 65	129
	53929.608	8,116 \pm 50	295
	53930.592	8,325 \pm 53	211
	53931.641	8,372 \pm 55	213
TWA 7	53327.632	12,419 \pm 51	197
N=13	53328.630	12,406 \pm 47	183
$\bar{RV} = 12,446 \pm 26$	53329.631	12,368 \pm 57	121
$\sigma = 94.18$	53419.453	12,349 \pm 52	195
	53420.469	12,445 \pm 48	291
	53421.436	12,495 \pm 50	232
	53422.442	12,513 \pm 51	204
	53480.294	12,720 \pm 50	220
	53686.641	12,398 \pm 52	158
	53741.575	12,402 \pm 52	180
	53742.546	12,454 \pm 52	187
	53743.549	12,421 \pm 51	188
	53744.523	12,403 \pm 48	220
TWA 8A	53327.636	8,610 \pm 52	175
N=15	53328.653	8,688 \pm 51	192
$\bar{RV} = 8,679 \pm 23$	53329.635	8,705 \pm 57	124
$\sigma = 90.07$	53419.473	8,555 \pm 50	243
	53420.484	8,542 \pm 52	183

Table 3 — *Continued*

Star	HJD - 2,400,000	Radial Velocity (m/s)	SNR
	53421.460	8,667 \pm 50	225
	53422.462	8,647 \pm 48	208
	53480.306	8,877 \pm 51	217
	53522.258	8,599 \pm 49	186
	53523.248	8,642 \pm 51	214
	53686.645	8,701 \pm 50	195
	53741.605	8,822 \pm 50	231
	53742.590	8,729 \pm 50	252
	53743.562	8,672 \pm 49	242
	53744.548	8,731 \pm 49	257
TWA 8B	53327.640	8,489 \pm 62	130
N=15	53328.650	8,523 \pm 63	126
$\bar{RV} = 8,607 \pm 32$	53329.639	8,453 \pm 63	122
$\sigma = 123.46$	53419.480	8,572 \pm 57	170
	53420.487	8,537 \pm 57	162
	53421.462	8,575 \pm 60	140
	53422.465	8,523 \pm 51	170
	53480.310	8,813 \pm 54	197
	53522.266	8,537 \pm 58	164
	53523.252	8,477 \pm 53	219
	53686.649	8,633 \pm 55	164
	53741.610	8,718 \pm 54	202
	53742.594	8,761 \pm 55	194
	53743.567	8,662 \pm 54	197
	53744.555	8,833 \pm 51	253
TWA 9A	53419.487	11,569 \pm 55	181
N=11	53420.493	11,633 \pm 54	191
$\bar{RV} = 11,649 \pm 21$	53421.466	11,574 \pm 53	155
$\sigma = 70.61$	53422.469	11,567 \pm 57	159
	53480.315	11,716 \pm 54	184
	53523.227	11,659 \pm 55	173
	53741.616	11,750 \pm 55	175
	53742.600	11,569 \pm 57	164
	53743.572	11,686 \pm 57	179
	53744.577	11,734 \pm 52	215
	54962.239	11,680 \pm 54	198
TWA 9B	53419.492	12,271 \pm 58	150
N=11	53420.497	12,320 \pm 54	175
$\bar{RV} = 12,279 \pm 27$	53421.470	12,101 \pm 58	144
$\sigma = 90.25$	53422.472	12,199 \pm 56	160
	53480.319	12,383 \pm 54	176
	53523.232	12,367 \pm 56	168
	53741.621	12,335 \pm 57	156
	53742.605	12,282 \pm 53	200
	53743.577	12,186 \pm 52	201
	53744.584	12,247 \pm 51	229
	54962.245	12,380 \pm 51	226
TWA 11B	53420.507	9,073 \pm 58	156
N=11	53421.444	8,782 \pm 55	191
$\bar{RV} = 8,923 \pm 58$	53421.487	8,719 \pm 55	184
$\sigma = 190.79$	53422.455	8,791 \pm 53	153
	53480.334	8,564 \pm 54	194
	53523.243	9,177 \pm 57	171
	53741.633	8,992 \pm 55	183
	53742.618	9,092 \pm 56	186
	53743.592	8,861 \pm 55	196
	53744.634	9,056 \pm 47	198
	54963.240	9,043 \pm 53	219
TWA 12	53328.641	12,276 \pm 54	255
N=12	53329.646	12,456 \pm 64	163
$\bar{RV} = 12,498 \pm 52$	53419.457	12,352 \pm 61	188
$\sigma = 180.79$	53420.479	12,708 \pm 57	209
	53421.450	12,420 \pm 56	228
	53422.459	12,445 \pm 60	188
	53480.297	12,302 \pm 60	186
	53686.664	12,445 \pm 58	196
	53741.592	12,370 \pm 60	188
	53742.557	12,655 \pm 60	196
	53743.558	12,758 \pm 59	192
	53744.530	12,789 \pm 62	190
TWA 13A	53327.646	11,889 \pm 57	158
N=14	53328.670	12,220 \pm 55	181
$\bar{RV} = 11,668 \pm 65$	53419.463	11,817 \pm 53	218
$\sigma = 241.66$	53420.472	11,488 \pm 56	172
	53421.454	11,469 \pm 55	181

Table 3 — *Continued*

Star	HJD - 2,400,000	Radial Velocity (m/s)	SNR
	53422.445	11,523 \pm 56	175
	53480.303	11,559 \pm 54	190
	53686.656	11,616 \pm 55	171
	53741.598	11,365 \pm 58	163
	53742.549	11,324 \pm 56	187
	53743.551	11,901 \pm 55	200
	53744.537	11,735 \pm 53	226
	54962.223	11,752 \pm 49	176
	54963.225	11,696 \pm 50	211
TWA 13B	53327.650	12,035 \pm 56	167
N=13	53328.673	11,677 \pm 58	150
$\bar{RV} = 12,075 \pm 41$	53419.468	12,130 \pm 53	209
$\sigma = 149.06$	53420.475	11,984 \pm 53	214
	53421.457	12,071 \pm 54	186
	53422.448	12,085 \pm 55	182
	53480.301	12,302 \pm 54	190
	53686.659	12,020 \pm 54	179
	53741.601	12,260 \pm 53	206
	53742.552	12,111 \pm 56	206
	53743.554	12,050 \pm 54	194
	53744.542	12,134 \pm 53	217
	54962.235	12,109 \pm 53	217
TWA 23	53419.500	4,445 \pm 61	244
N=14	53420.503	4,504 \pm 62	230
$\bar{RV} = 6,520 \pm 648$	53421.439	4,741 \pm 65	204
$\sigma = 2425.03$	53421.483	4,573 \pm 63	221
	53422.451	4,778 \pm 53	243
	53480.324	7,155 \pm 58	225
	53523.238	8,271 \pm 56	244
	53686.669	9,022 \pm 62	196
	53741.628	9,151 \pm 62	207
	53742.613	9,242 \pm 62	206
	53743.585	9,204 \pm 60	224
	53744.596	9,298 \pm 52	262
	54962.254	3,085 \pm 60	253
	54963.233	3,816 \pm 63	231

Note. — Reported values are Heliocentric radial velocities.